Nano Energy 81 (2021) 105633

Contents lists available at ScienceDirect

Nano Energy

journal homepage: http://www.elsevier.com/locate/nanoen

Full paper

Scaling-up perovskite solar cells on hydrophobic surfaces

Furkan H. Isikgor [a,*,1], Anand S. Subbiah [a,1], Mathan K. Eswaran [a], Calvyn T. Howells [a], Aslihan Babayigit [a,b], Michele De Bastiani [a], Emre Yengel [a], Jiang Liu [a], Francesco Furlan [a], George T. Harrison [a], Shynggys Zhumagali [a], Jafar I. Khan [a], Frédéric Laquai [a], Thomas D. Anthopoulos [a], Iain McCulloch [a], Udo Schwingenschlögl [a], Stefaan De Wolf [a,*]

[a] KAUST Solar Center (K.S.C.), Division of Physical Sciences and Engineering (P.S.E.), King Abdullah University of Science and Technology (KAUST), Thuwal 23955-6900, Saudi Arabia
[b] IMEC, division Institute for Materials Research (IMO-IMOMEC), Wetenschapspark 1, 3590 Diepenbeek, Belgium

ARTICLE INFO

Keywords:
Perovskite solar cell
Scalable
Large area
Hydrophobic PTAA substrate
Binding energy
Pinholes

ABSTRACT

Despite impressive power conversion efficiencies (PCEs) reported for lab-scale perovskite solar cells (PSCs), obtaining large-area devices with similar performance remains challenging. Fundamentally, this can largely be attributed to a polarity mismatch between the perovskite-precursor solution and the underlying hydrophobic contact materials, resulting in perovskite films of insufficient quality for scaled devices. Specifically, for *p-i-n* devices, the commonly used DMF/DMSO co-solvent has a significant polarity mismatch with its underlying hole-transporting layer, PTAA. Here, the role of $MAPbI_3$•solvent adduct interaction with the PTAA surface towards the formation of micro- and nano-scale pinholes is elucidated in detail. Replacing DMSO with NMP in the co-solvent system changes the binding energy profoundly, enabling uniform and dense films over large areas. The PCE of DMF/NMP ink-based devices drops slightly with increasing active device area, from 21.5% (0.1 cm^2) to 19.8% (6.8 cm^2), in comparison with conventional DMF/DMSO ink. This work opens a pathway towards the scalability of solution-processed perovskite optoelectronic devices.

1. Introduction

Solution-processable photovoltaic technologies have gained significant traction recently, with perovskite solar cells (PSCs) at the forefront, reporting a champion power conversion efficiency (PCE) of 25.5% [1]. In terms of lab-scale device efficiency, this value is competitive with market-established technologies. However, to be commercially relevant, the scalability of PSCs is a crucial aspect. Though numerous reports establish highly efficient PSCs with millimeter-scale active areas, the PCE of PSCs plummets upon increasing the active area, in comparison to other proven technologies; the efficiencies typically fall below 18% when the active area of the device is greater than 1 cm^2, regardless of the deposition technique [1–4]. This loss in PCE is due to several factors such as increasing series resistance, lower shunt resistance, but primarily due to non-uniformity of the material stack over large areas [2,4,5]. Therefore, research must focus on developing strategies towards scalable, high-performance perovskite devices with minimal losses, for a successful transition of the technology from the laboratory to industry.

Alongside these technological challenges, materials costs of all device layers also play a crucial role in scaling-up PSCs. Employing organic charge transport layers allows for low-temperature processed dopant-free PSC manufacturing and uses established organic electronics manufacturing processes [6,7]. Consequently, the inverted *p-i-n* architecture, which uses organic materials both for its electron and hole transport layers (ETLs and HTLs), holds great promise for large-area PSCs [8,9]. Motivated by these arguments, herein, we study the scalability of the *p-i-n* device architecture, with specific attention for uniform methylammonium lead triiodide ($MAPbI_3$) perovskite deposition on the organic poly(triarylamine) (PTAA) HTL.

PTAA has been a widely used HTL in inverted *p-i-n* PSCs. However, its hydrophobic nature and low surface free energy have been a persistent challenge for obtaining uniform deposition of perovskites over larger areas [10–14]. Perovskite solution processing is often based on N, N′-dimethylformamide/dimethyl sulfoxide (DMF/DMSO) solvent blends, combined with subsequent anti-solvent extraction. This methodology enables highly efficient *n-i-p* devices, where the

* Corresponding authors.
E-mail addresses: furkan.isikgor@kaust.edu.sa (F.H. Isikgor), stefaan.dewolf@kaust.edu.sa (S. De Wolf).
[1] Both authors contributed equally to this work.

https://doi.org/10.1016/j.nanoen.2020.105633
Received 7 August 2020; Received in revised form 27 October 2020; Accepted 21 November 2020
Available online 25 November 2020
2211-2855/© 2020 Elsevier Ltd. All rights reserved.

perovskite-precursor inks interact with hydrophilic metal-oxide surfaces (SnO_2, TiO_2, Nb_2O_5). However, important questions remain over their efficacy on hydrophobic PTAA substrates [10,15]. Previous studies have already enunciated the precursor interaction with hydrophobic PTAA surfaces, leading to a reduced nucleation density, thereby enabling large-grained perovskite absorber films, resulting in highly efficient small-area devices [12]. However, this interaction results in micro- and nano-scale pinholes in the perovskite absorber. Such pinholes result in more significant deviations in PCE for small-area devices; for large-area devices, this lowers their overall PCE [10,15]. This underlines the critical need for more fundamental insights on the nature of events occurring at this interface.

This study investigates perovskite thin-film formation on hydrophobic PTAA surface in detail by combining experimental results with density functional theory (DFT) calculations and classical nucleation theory. The calculations show that binding energies and the electronic interaction of the perovskite•solvent adduct play a crucial role in perovskite film formation on hydrophobic PTAA as HTL. We identify DMSO to be the main culprit for the formation of micro- and nano-scale pinholes when the perovskite layer is solution-processed from the commonly used DMF/DMSO ink. To alleviate this issue, DMSO is replaced with NMP. We identify several advantages of NMP over DMSO, particularly for the fabrication of large-area PSCs. Firstly, with the DMF/NMP ink system, the resultant $MA^+PbI_3^-$•NMP adduct has a considerably higher binding energy (− 0.728 eV) with the underlying PTAA HTL than that of the $MA^+PbI_3^-$•DMSO adduct (− 0.143 eV). The high $MA^+PbI_3^-$•NMP—PTAA binding energy inhibits the receding of the adduct from the PTAA surface due to interfacial tension and, consequently, suppresses the formation of micro-scale pinholes. Secondly, the $MA^+PbI_3^-$•NMP—PTAA binding energy (− 0.728 eV) is significantly higher than the self-binding energy of NMP (− 0.180 eV), which is not the case when DMSO is used (the DMSO—DMSO self-binding energy is − 0.340 eV). Hence, the NMP adduct has a significantly lower interfacial energy with PTAA, which increases the nucleation density of perovskite on PTAA and, consequently, suppresses nano-scale pinhole formations.

To illustrate the efficacy of replacing DMSO with NMP, we show systematic variations in the photovoltaic device performance with increasing active area. The champion PCEs of the DMSO-based *p-i-n* PSCs significantly drops from 20.4% to 13.4% and 12.6%, respectively for 0.1 cm^2, 1.0 cm^2, and 2.0 cm^2 devices, due to the existence of macro- and nano-scale pinholes. On the other hand, the PCE of the NMP-based devices drops only ~1% from 21.4% when the active device area increased from 0.1 cm^2 to 2.0 cm^2. With a significant improvement with the increasing active area, we further employ NMP-based inks to fabricate mini-modules with four sub-cells using the P_1-P_2-P_3 scribing strategy with an active area of 6.8 cm^2. The best mini-module delivers a PCE of 19.8% with a very high reproducibility. These results highlight that the absolute PCE value of our NMP-based devices drops only ~0.9% when the active area increases by an order of magnitude, being very close to that of current commercial photovoltaic technologies (~0.8%). On the other hand, in current literature, PSC champion devices employing *n-i-p* and *p-i-n* device architectures exhibit a ~3.2% and ~ 2.0% drop in absolute PCE for an order of change in device active area. Hence, a comprehensive understanding of the ink-substrate interaction provided in this study may provide crucial insights towards scaling-up PSCs, particularly on hydrophobic charge-transporting layers.

2. Results and discussion

2.1. DFT calculations

The chemical structure of the precursor constituents plays a vital role in the wetting properties of the perovskite ink on the hydrophobic PTAA surface. Here, we make use of DFT calculations to understand the interaction of $MA^+PbI_3^-$•solvent adducts with PTAA polymer. The choice of a simple perovskite system in the form of $MAPbI_3$ enables a fundamental understanding of the interaction of the precursor ink with hydrophobic surfaces, eliminating the synergistic crystallization effects of different ions [16,17]. The calculated molecular electrostatic potential maps (Fig. 1**A**) show the electron-withdrawing nature of oxygen atoms in the solvent molecules employed in this study (DMF, DMSO, and NMP (n-methyl-2-pyrrolidone)), rendering them polar. Also, $MAPbI_3$ is relatively more polar than the individual solvent molecules (Fig. 1**B**), majorly due to the electrostatic interaction between the highly electron-deficient MA^+ and the electron-rich PbI_3^- ions. Upon mixture, the MA^+ and PbI_3^- ions interact with the electron-cloud of the solvent systems, resulting in $MA^+PbI_3^-$•DMF, $MA^+PbI_3^-$•DMSO, and $MA^+PbI_3^-$•NMP adducts [18]. This interaction ensures the solvation of the perovskite precursors in polar aprotic solvents, and the calculations (Fig. 1**C**) show an enhancement of the polarization due to the formation of the adducts. The establishment of heavily polarized electron-rich and -poor domains in $MA^+PbI_3^-$•solvent adducts ensues the perovskite ink to be hydrophilic.

On the other hand, the electrostatic potential map of PTAA illustrates weak polarizability (Fig. 1**D**). The bulky, non-polar triaryl units shield the nitrogen core of the polymer, resulting in a non-polar aromatic surface. This phenomenon relates to the well-known hydrophobic character of PTAA, and its high water contact-angle (~94°) in comparison to other known HTLs in the literature (Fig. S1). Our calculations highlight the substantial mismatch in polarizability between perovskite ink and substrate, summarizing the problem at hand for depositing perovskite on PTAA substrates. Fig. S1 shows photographs of $MAPbI_3$ absorber fabricated on different substrates using DMF/DMSO (4:1) co-solvent composition. The coatings on PTAA substrates stand out, as one could observe a noticeable number of micro-scale pinholes on them (Fig. S1E). However, $MAPbI_3$ deposited on hydrophilic SnO_2, NiO_x, and PEDOT:PSS substrates produces highly specular, visually continuous films. The changes in film quality indicate that DMF/DMSO-based ink compositions that enable good quality perovskites on hydrophilic substrates (high surface free energy) may not do so on hydrophobic substrates (low surface free energy). Fig. S2 shows a significant difference in surface free energies of PTAA (43.6 mN/m) and NiO_x (69.1 mN/m) substrates; more importantly, the polar component of PTAA is close to zero.

To gain further insights into pinhole formation, we study the binding energies of $MA^+PbI_3^-$•solvent adducts with the PTAA surface. Fig. 1 **(E–G)** highlights the variations in electrostatic potential maps upon interaction of $MA^+PbI_3^-$•DMF, $MA^+PbI_3^-$•DMSO, and $MA^+PbI_3^-$•NMP adducts with PTAA. The DMSO adduct shows the lowest binding energy (− 0.143 eV) with the PTAA surface, in comparison with DMF (− 0.679 eV) and NMP (− 0.728 eV) adducts. Fig. 1**(E–G)** also compares the corresponding contact angles of $MAPbI_3$ precursor ink (with DMF, DMSO, and NMP solvents) on PTAA substrates, showing a trend similar to the calculated binding energies. The red circle in Fig. 1E indicates the delocalization of the electron cloud around the oxygen atom of the DMF molecule, which makes PTAA more polar. The interaction of $MA^+PbI_3^-$•NMP with PTAA follows a similar trend, where the electron cloud of the oxygen atom in NMP delocalizes. However, with DMSO, the electron-rich cloud remains local at its oxygen atom, indicating a weaker interaction with the PTAA surface. This weak interaction is evident when fabricating $MAPbI_3$ thin films using pure DMSO solvents with anti-solvent extraction. The low binding energy results in a complete washing away of the precursor ink from the PTAA film, i.e. no film formation. Fig. S3 compares photographs of perovskite thin films fabricated using DMF, DMSO, DMF/DMSO, and DMF/NMP solvent blends. The complex interplay of $MA^+PbI_3^-$•DMSO with PTAA seems to be the principal culprit for the non-uniform coating of the perovskite from a typical DMF/DMSO (4:1) ink, featuring numerous pinholes. Replacing DMF/DMSO (4:1) with DMF/NMP (6:1) ink optimized in this study results in a uniform film with no visible signs of pinholes (Fig. S3).

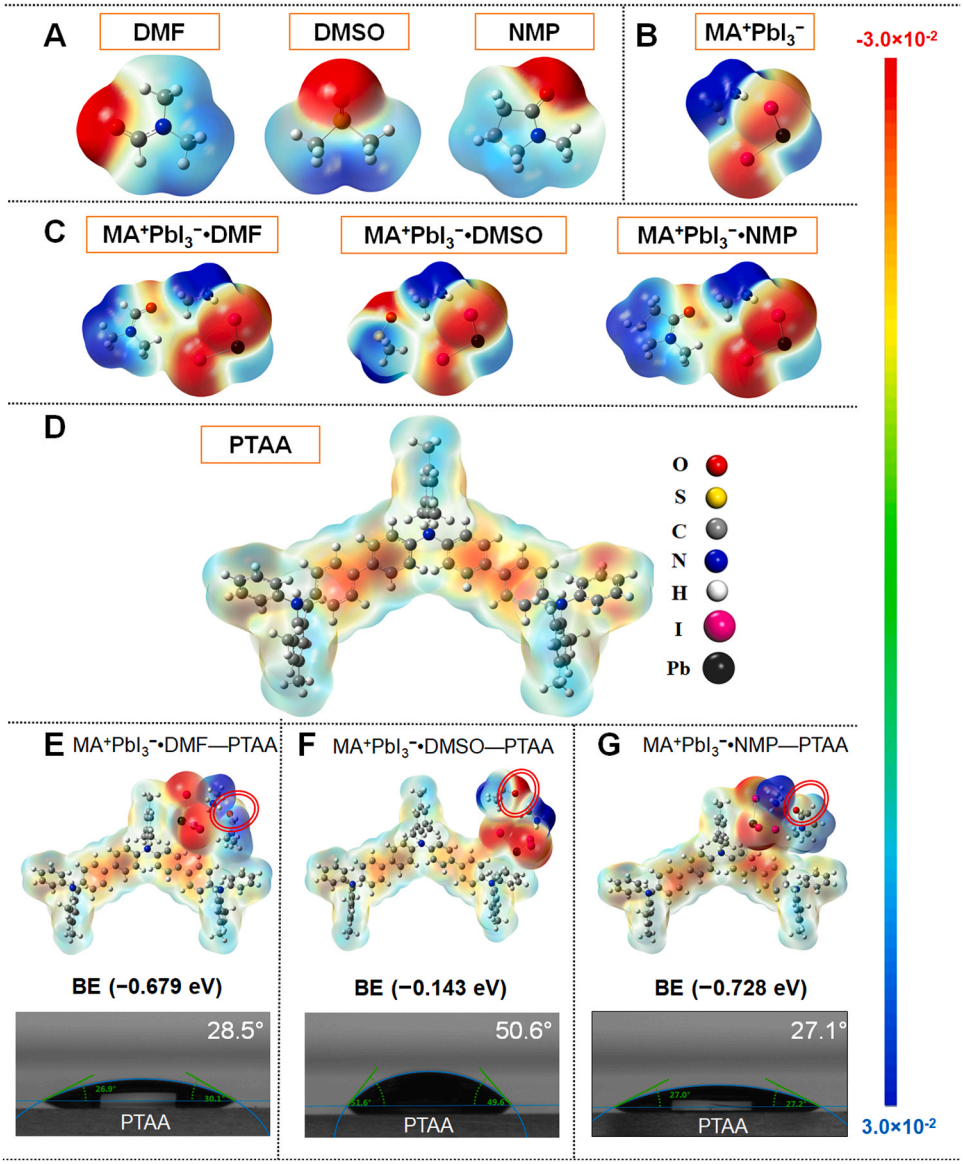

Fig. 1. Electrostatic potential maps and binding energy. Molecular electrostatic potential maps of the (**A**) solvents DMF, DMSO, and NMP, (**B**) ionic components MA^+ and PbI_3^- formulating $MAPbI_3$, (**C**) $MA^+PbI_3^-$•DMF, $MA^+PbI_3^-$•DMSO, and $MA^+PbI_3^-$•NMP adduct complexes, and (**D**) PTAA molecule. (• indicates interaction between $MAPbI_3$ and the solvent system). Binding energy and electrostatic potential maps of (**E**) $MA^+PbI_3^-$•DMF—PTAA, (**F**) $MA^+PbI_3^-$•DMSO—PTAA, and (**G**) $MA^+PbI_3^-$•NMP—PTAA (— indicates interaction between $MA^+PbI_3^-$•solvent adduct and substrate) with contact angle measurements for 1.1 M precursor solutions of the corresponding solvents on a PTAA surface. (For interpretation of the references to colour in this figure legend, the reader is referred to the web version of this article.)

2.2. *Eliminating micro-scale pinhole formation*

Fig. 2**A** schematically compares the micro-scale pinhole formation mechanism in $MAPbI_3$ thin films by employing DMF/DMSO ink for an optimized ratio (v/v) of 4:1 on PTAA surfaces; [10,19] we note that the DMF/DMSO (4:1) precursor formulation has been a critical enabler for high-quality perovskite deposition on hydrophilic surfaces in perovskite literature [20]. This schematic also illustrates the formation of pinhole-free $MAPbI_3$ thin films using the DMF/NMP ink for an optimized ratio (v/v) of 6:1 (Fig. S4). The difference between the optimized ratios of the DMF/DMSO (4:1) and DMF/NMP (6:1) solvent blends stems from the complex interplay of binding energy (Fig. 1) and solubility limit (Fig. S10) of the perovskite precursors in these co-solvents.

Introducing small volume fractions of DMSO in the DMF solvent slows down the crystallization of $MAPbI_3$ thin film considerably. Earlier studies have shown that the relatively high vapor pressure of DMF and its weaker coordination with $MA^+PbI_3^-$ results in the rapid removal of DMF upon anti-solvent extraction [18,20–22]. Table S1 lists the crucial solvent parameters of DMF, DMSO, and NMP for reference. However, the low vapor pressure of DMSO and the high binding energy of $MA^+PbI_3^-$•DMSO adduct (− 0.481 eV) results in a stable intermediate wet-film. Later, annealing the samples initiates nucleation and crystallization.

Even though the contact angle of the DMF/DMSO ink on PTAA initially seems favorable (34.2°, Fig. 2**A**), the anti-solvent quenching alters the ink/substrate dynamics significantly, as it establishes $MA^+PbI_3^-$•DMSO adduct formation [18]. As mentioned earlier, the low binding energy of $MA^+PbI_3^-$•DMSO with PTAA (− 0.143 eV) plays a critical role in the partial de-wetting of the intermediate wet film from the hydrophobic PTAA surface. At this point, local and random de-wetting of the $MA^+PbI_3^-$•DMSO intermediate film takes place despite the centrifugal force from spin-coating. Additionally, the self-binding energy of DMSO—DMSO (− 0.340 eV) is considerably higher than that of $MA^+PbI_3^-$•DMSO—PTAA (− 0.143 eV), aiding in the repulsion of intermediate film from PTAA surface. Table S2 tabulates the binding energies of various complexes calculated for this study. The process of $MA^+PbI_3^-$•DMSO adduct receding from the surface of PTAA due to interfacial tension is evident from the formation of visible micro-scale pinholes in the intermediate wet film (Fig. S5A). We note that micro-scale pinhole formation is independent of perovskite nucleation and growth processes, as they exist before the annealing step. Subsequent thermal annealing releases DMSO molecules, retaining the pinholes in the $MAPbI_3$ absorber film (Fig. S5B and S5C). The micro-scale pinholes are visible on large-area $MAPbI_3$ devices (highlighted as

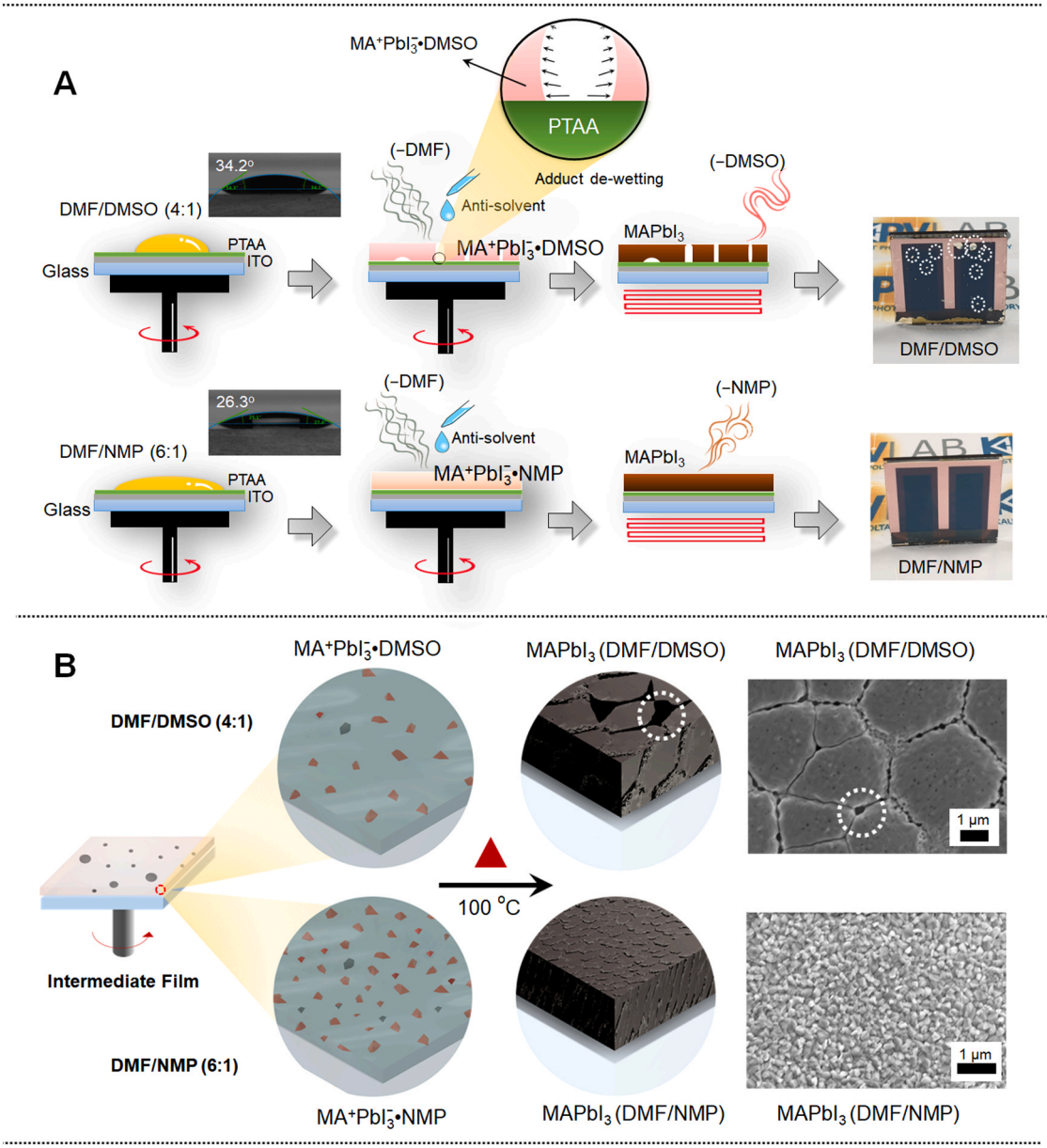

Fig. 2. Schematic representation of micro and nano-scale pinhole formation. (**A**) $MAPbI_3$ perovskite thin film formation by using the DMF/DMSO and the DMF/NMP ink. The de-wetting of $MA^+PbI_3^-$•DMSO adduct on PTAA surface results in micro-scale pinholes. Photographs with white circles highlight micro-scale pinhole formation in the completed device (active area: 2 cm^2) for DMF/DMSO, whereas the DMF/NMP-based device is completely micro-scale pinhole-free. (**B**) Schematic alongside SEM image illustrating nano-scale pinhole formation (white circles) in DMF/DMSO-based perovskite thin films despite larger grain size, whereas the DMF/NMP ink offers uniform thin films.

white circles) fabricated using DMF/DMSO ink, even without the help of an optical microscope.

One of the motivations to replace DMSO with NMP to achieve a strong interaction with the PTAA surface is that NMP is known to recover certain hydrocarbons such as 1,3-butadiene and acetylene, in the processing of petrochemicals [23]. Moreover, its low vapor pressure, high donor number (Table S1), and strong coordination towards the perovskite precursors ($MA^+PbI_3^-$•NMP binding energy − 0.336 eV, Table S2), allows it to preserve the decelerated crystallization of $MAPbI_3$ thin films. The contact angle of DMF/NMP ink on PTAA (~26.3°) is relatively small in comparison with its DMF/DMSO counterpart (Fig. 2**A**). Upon removal of DMF via anti-solvent extraction, the binding of $MA^+PbI_3^-$•NMP with PTAA (− 0.728 eV) seems sufficiently high to keep the intermediate phase intact. More importantly, the self-binding energy of NMP (− 0.180 eV) is low in comparison with the $MA^+PbI_3^-$•NMP—PTAA binding energy. This improved binding energy results in a stable intermediate wet film with a robust interaction with the underlying PTAA layer, which upon annealing results in compact-uniform films. As a result, the use of the DMF/NMP ink allows for the deposition of highly continuous and shiny $MAPbI_3$ absorber layer on hydrophobic PTAA surface, in comparison to the films with micro-scale pinholes obtained from DMF/DMSO ink (Fig. S3C and S3D).

2.3. *Eliminating nano-scale pinhole formation*

Another aspect of fabricating $MAPbI_3$ thin films using DMF/DMSO inks on hydrophobic PTAA is the formation of nano-scale pinholes in addition to the micro-scale pinholes. Fig. 2**B** shows that though DMF/DMSO ink results in large-grained perovskite films, they incorporate voids in the nano-scale regime at grain boundaries (highlighted with

white circles). Annealing the $MA^+PbI_3^-$•DMSO intermediate film removes DMSO from the wet film, leading to nucleation and growth processes for the formation of the polycrystalline $MAPbI_3$ film. From the perspective of classical nucleation theory, the morphology of the perovskite film is highly dependent on the nucleation density of the perovskite clusters on the PTAA surface. Eq. (1) describes the change in Gibbs free energy ΔG required for the nucleation process.

$$\Delta G(r) = \left(-\frac{4\pi r^3}{3V_M}\right) RTln(S) + 4\pi r^2 \gamma_{CL} \quad (1)$$

where r is the radius of the spherical perovskite cluster, γ_{CL} is the interfacial energy between the liquid and the cluster, V_M is the molar volume of the nucleus, and S is the supersaturation ratio defined as $S = C/C_s$ (C: the solute concentration, C_s: the solubility limit). For the nucleation process to commence ($d(\Delta G)/dr = 0$), the critical energy barrier (ΔG^*) and critical radius (r^*) for nucleation are defined as:

$$\Delta G^* = \frac{16\pi V_M^2 \gamma_{CL}^3}{3R^2T^2(lnS)^2} \quad r^* = \frac{2V_M\gamma_{CL}}{RTlnS} \quad (2)$$

For the heterogeneous nucleation, as in this case, the energy barrier (ΔG^*) is reduced through interface energy as a function of contact angle ($\Delta G^*.f(\theta)$) [24]. The above equations highlight the role of interfacial energy (γ_{CL}) and supersaturation ratio (S) in overcoming the energy barrier for nucleation [25]. With the typical DMF/DMSO ink, the $MA^+PbI_3^-$•DMSO—PTAA binding energy is low in comparison with DMSO—DMSO, leading to a high interfacial energy between the wet film and PTAA. This consequently results in an overall increase in r* and ΔG^*. Higher values of the critical energy barrier and critical radius implicate a low nucleation density, which in turn substantiates the large $MAPbI_3$ grains (~2-5 μm diameter) obtained for DMF/DMSO ink (Fig. S6A). Despite the larger grains, the low nucleation rate results in grain boundaries that are poorly connected and spaced out, thereby giving rise to the nano-sized pinholes (Fig. 2**B**).

To circumvent this issue, the PTAA substrate is pre-wetted with DMF to allow some pre-adsorption of the solvent on the PTAA surface [10, 26]. The pre-wetting lowers the interfacial energy between the PTAA and the $MA^+PbI_3^-$•DMSO adduct, and notably, the process improves the nucleation density. Upon annealing, the packing density of $MAPbI_3$ grains improves; however, the grain size drops to a few hundreds of nm (Fig. S6B). Although the DMF pre-wetting proves to be an effective strategy to eliminate nano-scale pinholes, the process does not mitigate the formation of micro-scale pinholes, as they originate from $MA^+PbI_3^-$•DMSO de-wetting even before the initiation of the nucleation process. Evidently, one could observe the presence of these micro-scale pinholes on $MAPbI_3$ (DMF/DMSO) devices even after employing DMF pre-wetting step (white circles Fig. 2**A**). Moreover, the evaporation of DMF from the PTAA surface after pre-wetting introduces temporal variations in nucleation density for $MAPbI_3$ growth, which in turn leads to the formation of buried pinholes. Fig. S7A (white circles) highlights the formation of buried pinholes in DMF/DMSO based $MAPbI_3$ devices, where the fabrication process involves DMF pre-wetting. The issue of buried pinholes is often over-looked in literature; however, their presence affects the device interface adversely, leading to poor device performance.

Introducing the DMF/NMP ink suppresses the formation of nanoscale pinholes completely and results in continuous $MAPbI_3$ thin films with small grains (~100 nm) (Figs. 2**B** and S8). Replacing DMSO with NMP reduces the interfacial energy of the intermediate film with PTAA, as the $MA^+PbI_3^-$•NMP—PTAA binding energy is significantly higher than the self-binding energy of NMP. As per Eq. (2), NMP lowers ΔG^* and r* values, resulting in a high nucleation density. In correlation, the $MA^+PbI_3^-$•NMP adduct film takes a brownish tinge after anti-solvent extraction, indicating the initiation of nucleation and growth processes, even before thermal annealing (Fig. S9). Another critical factor that lowers ΔG^* is the solubility limit of $MAPbI_3$ in DMF/NMP (6:1 v/v) (~2.1 M), being considerably less than that of DMF/DMSO (4:1 v/v) (~2.6 M) (Fig. S10). As a consequence, NMP incorporation results in uniform and tightly packed $MAPbI_3$ films with smaller grains, while simultaneously eliminating the need for a pre-wetting step and preventing the formation of micro- and nano-sized pinholes. Further enhancements in the optoelectronic properties, film roughness, energy band alignment, and trap densities of $MAPbI_3$ thin films fabricated using the DMF/NMP ink in comparison with the conventional DMF/DMSO ink are described briefly in the methods section and the corresponding figures are presented in the Supplementary Information (Figs. S20–S29 and Tables S5 and S6). Briefly, our results show closely packed small grains without pinholes can indeed work better than loosely packed large grains with pinholes. In the second case, pinholes arising from the spatial distance and reduced packing density between the grains result in shunt pathways, which drop the PCE of the devices considerably. However, as reported in previous studies, closely packed pinhole-free large grains perform better than their small grain counterparts due to the reduced grain boundaries and trap states [27–29]. These results indicate that the PCEs reported here with NMP-based devices can be further improved by increasing the grain size, satisfied if the grains are pinhole-free and closely packed.

2.4. Scaling-up $MAPbI_3$ p-i-n devices

To further consolidate our understanding, we fabricate $MAPbI_3$ solar cells in the *p-i-n* architecture (ITO (indium doped tin oxide)-PTAA-$MAPbI_3$-C_{60} (fullerene)-BCP (bathocuproine)-Ag (silver)) from both DMF/DMSO (D/D) and DMF/NMP (D/N) inks. Fig. 3**(A–D)** compares the device parameters of 96 devices with an active area of 0.1 cm^2 for both conditions. For this study, we employed DMF pre-wetting for the fabrication of the $MAPbI_3$(D/D) based devices, as fabricating without this additional step renders these devices inefficient (Fig. S11). Fig. 3**A** shows that both $MAPbI_3$(D/D) and $MAPbI_3$(D/N) based devices exhibit PCEs above 20% for small-area devices (0.1 cm^2). However, the DMF/DMSO based devices display a wide PCE distribution with an average PCE of 15.2% and a large standard deviation of ± 5.7% (Fig. 3**E**). Interestingly, nearly 27% of the devices fabricated using the popular DMF/DMSO ink cannot surpass a PCE higher than 10%, giving a difference of more than 5% in performance between the champion and average PCE. The statistics of DMF/DMSO based devices stand as a clear testimony to the irregularities in $MAPbI_3$ film across the small-area device pixels. Most strikingly, the formation of micro- and nano-scale pinholes directly impacts the open circuit potential (V_{OC}) and fill factor (FF) distribution of DMF/DMSO devices (Fig. 3**C** and 3**D**). However, the short-circuit current density (J_{SC}) and the short-term stability under maximum power point tracking are not significantly influenced, which is further supported by external quantum efficiency (EQE) measurements (Figs. S12 and S13). The buried pinholes, as described earlier, can lead to an increased trap state density, inefficient charge collection, and, therefore, poor device performance. On the other hand, DMF/NMP based devices exhibit an average PCE of 19.2%, with a significantly reduced standard deviation of ± 2.1%. Eliminating the formation of micro- and nano-scale pinholes have a major impact on the device statistics of DMF/NMP devices, showing promise towards scalability.

To illustrate the impact of negating micro- and nano-scale pinholes of $MAPbI_3$ on PSCs, particularly for the uniformity of large-area devices, we also fabricated PSCs with different active areas, i.e., 0.5 cm^2, 1.0 cm^2, and 2.0 cm^2 (Table S3 and Figs. S14–S16). Fig. 3**(E–F)** displays PCE histograms comparing 0.1 cm^2, 1.0 cm^2, and 2.0 cm^2 devices obtained from both DMF/DMSO and DMF/NMP inks. The impact of the solvent systems on the reproducibility and increasing device area on PTAA substrates is evident from these histograms. The difference in average PCE ($PCE_{(D/N)}$–$PCE_{(D/D)}$) from the histograms varies from 4% to 10.1% and 11.2% when increasing device areas from 0.1 cm^2 to 1.0 cm^2 and 2.0 cm^2. Fig. 3**(H–J)** shows the champion devices obtained from both inks for the different device areas. The champion small area device

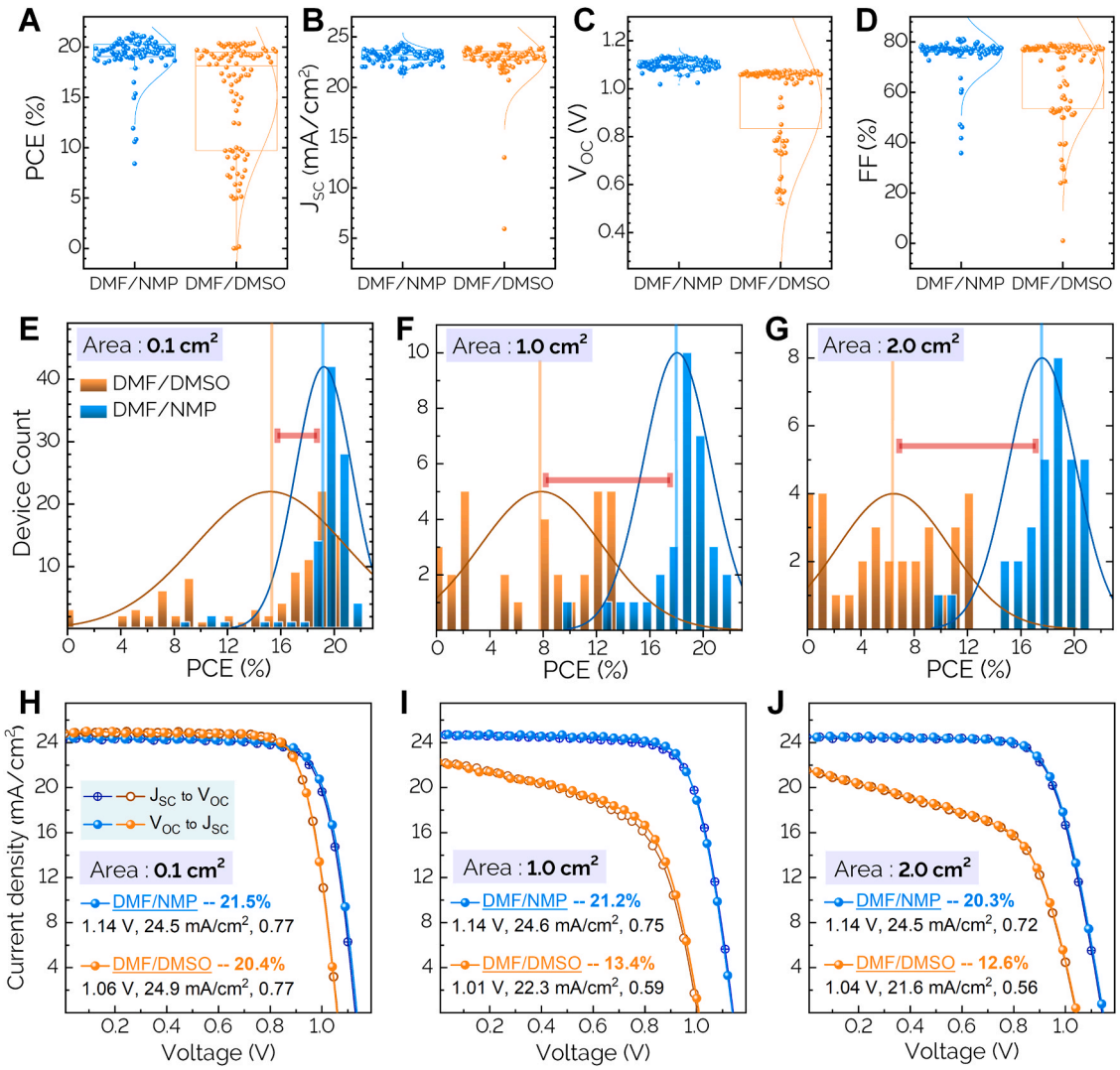

Fig. 3. Performance comparison of $MAPbI_3$ perovskite solar cells from DMF/DMSO and DMF/NMP inks. Box histogram comparing the device parameters of *p-i-n* $MAPbI_3$ devices on PTAA substrates fabricated using DMF/DMSO and DMF/NMP inks: (**A**) PCE, (**B**) J_{SC}, (**C**) V_{OC}, and (**D**) FF. PCE statistics of DMF/DMSO and DMF/NMP based devices for active device areas of (**E**) 0.1 cm^2 (96 devices), (**F**) 1.0 cm^2 (32 devices), and (**G**) 2.0 cm^2 (32 devices). (**H–J**) Corresponding current-voltage characteristics under AM 1.5 G illumination of the champion devices.

using the DMF/NMP ink can deliver a PCE of 21.4% with a V_{OC} of 1.135 V, J_{SC} of 24.39 mA/cm^2, and FF of 0.77; this PCE is amongst the highest reported for *p-i-n* perovskite solar cells. The DMF/DMSO based cells exhibit a champion PCE of 20.4%, which is 1% absolute lower than the DMF/NMP based devices, and the loss in performance is due to a lower V_{OC} of 1.06 V (J_{SC} and FF are comparable). Upon increasing the active area up to 1.0 cm^2 and 2.0 cm^2, the DMF/NMP-based devices preserve their V_{OC} and J_{SC}, highlighting the excellent optoelectronic quality of the $MAPbI_3$ film. More specifically, the corresponding champion devices deliver a PCE of 21% and 20% for 1.0 cm^2 and 2.0 cm^2 active areas, respectively. The decrease in performance is solely due to losses in FF. We, therefore, believe it mainly stems from the increasing sheet resistance of the ITO. The corresponding champion devices obtained from the DMF/DMSO ink show a PCE of 13.4% and 12.6% for 1.0 cm^2 and 2.0 cm^2 devices, respectively. With significant performance losses in J_{SC}, V_{OC}, and FF, as extracted from the JV-curves, the obvious low shunt resistance and high series resistance in these devices are linked to the presence of micro-scaled and buried pinholes in the absorber as mentioned before.

As the large-area devices with an active area of 2 cm^2 show promise, we also employed the DMF/NMP ink to fabricate mini-modules with four sub-cells using P_1-P_2-P_3 scribing strategy with an active area of 6.8 cm^2. Fig. 4**A** depicts the schematic of mini-modules employed to fabricate *p-i-n* $MAPbI_3$ devices using DMF/NMP ink. A thin strip of 50 nm gold is deposited on ITO substrates to reduce the series resistance, as depicted in the design layout (Fig. S17). The design of sub-cells shaped as small rectangular patches aids in improving the fill-factor of the mini-modules, by limiting the series resistance of the device. Fig. 4**B** shows the champion IV characteristics of the mini-module with a PCE of 19.8%, a FF of 72.7%, and V_{OC} of 4.45 V for four sub-cells. All devices of the mini-module show considerable performance with an average PCE of 17.9% for 14 devices (Fig. S18).

Fig. 4**C** portrays the minimal change in PCE statistics for DMF/NMP based devices with increasing active area. On the contrary, Fig. S19 depicts a significant drop in average PCE, where DMF/DMSO is used to fabricate large devices. Fig. 4**D** compares the results obtained in this study with state-of-the-art large area devices reported in the literature (Table S4). Different photovoltaic technologies (except for PSCs) follow an apparent empirical inverse scaling law [4], with their absolute PCE value decreasing by about 0.8% when the device area increases by one order of magnitude. In current literature, PSC champion devices employing *n-i-p* and *p-i-n* device architectures exhibit a ~3.2% and

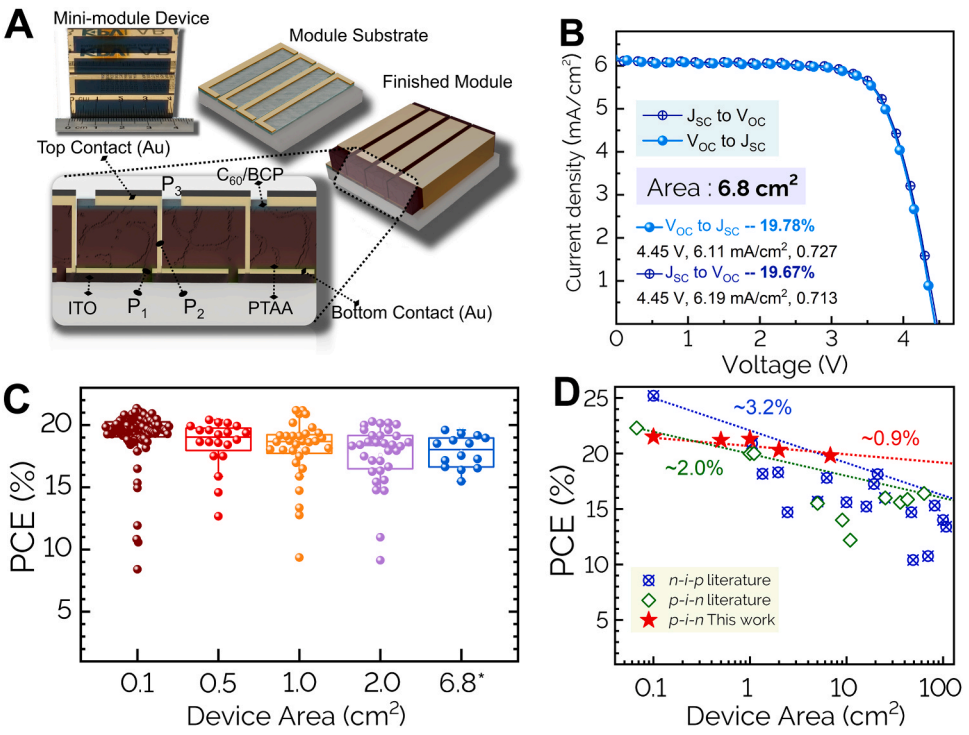

Fig. 4. Mini-modules and PSC scalability. (**A**) Schematic representation of device architecture depicted alongside bottom substrates and finished modules of *p-i-n* $MAPbI_3$ mini-modules employing P_1-P_2-P_3 strategy. (**B**) Champion IV characteristics of mini-module with a sub-cell area of 1.7 cm^2 and an overall active area of 6.8 cm^2 showing a PCE of 19.78%. (**C**) Histogram depicting a minimal change in PCEstatistics over a scalable active area (0.1–6.8 cm^2) without cherry-picking devices, elucidating the negation of pinhole formation by employing DMF-NMP inks over large-area. (**D**) Comparison of PCE of various champion perovskite devices in literature with larger active-areas illustrating the importance of this work in terms of scalability. The slope of the fitted lines depicts the loss in absolute PCE for an order of magnitude change in device active area, from champion devices in current literature (3.2% and 2.0% for *n-i-p* and *p-i-n*) and in this work (0.9% for *p-i-n*). (References are tabulated in Table S4).

~2.0% drop in absolute PCE for an order of change in device active area (Fig. 4**D**). In this study, we demonstrate for the first time that PSC indeed is competitive with other technologies where the absolute value of PCE drops ~0.9% when the active area increases by order of magnitude.

3. Experimental section/methods

3.1. Materials

Patterned indium tin oxide (ITO) glass substrates (15 $\Omega.\square^{-1}$) were supplied by Xinyan Technology Ltd. Poly(triaryl amine) (PTAA, 99.999% purity) was obtained from Xi'an polymer. Methylammonium iodide (MAI) was received from Dyesol Ltd. Lead (II) iodide (PbI_2: 99.999% purity) was received from Alfa Aesar. Other chemicals, C_{60} (98% purity), chlorobenzene (CB, anhydrous, 99.8% purity), dimethylformamide (DMF, anhydrous, ≥ 99.8% purity), dimethyl sulfoxide (DMSO, anhydrous, ≥ 99.9% purity), N-methyl-2-pyrolidone (NMP, anhydrous, ≥99.8% purity), ethyl acetate (EtAc, anhydrous, 99.8% purity), bathocuproine (BCP, 99.99% purity) and silver (Ag shot, ≥ 99.99% purity) were purchased from Sigma-Aldrich. All materials were used as received without further purification.

3.2. Solar cells fabrication and characterization

The inverted (*p-i-n*) device stack consists of ITO-PTAA-$MAPbI_3$-C_{60}-BCP-Ag. The devices were prepared using the following procedure. ITO glass substrates were cleaned by sonication successively in detergent, deionized water, acetone, and isopropanol. The sonication time was 15 min for each cleaning. They were then dried with N_2 flow and transferred to a glovebox filled with N_2. Au patterns (50 nm thick) were deposited to decrease the ITO series resistance for fabrication of large-area devices. To coat the PTAA HTL, 6 mg of PTAA was dissolved in 3 ml of CB to obtain a 2 mg/ml PTAA solution. The solution was spin-coated on top of the ITO substrates at 6,000 rpm for 20 s and subsequently annealed at 100 °C for 10 min to obtain a PTAA thin film with a thickness of ~20 nm. The perovskite precursor solutions were prepared by dissolving equimolar of PbI_2 and MAI (1.1 M) in co-solvents of DMF/DMSO or DMF/NMP. The perovskite inks were then coated onto the PTAA layer by using a consecutive two-step spin-coating process consisting of 2k rpm for 10 s and 5k rpm for 30 s 300 μl of EtAc was dropped at the 10th s of the second step. The films were then annealed at 100 °C for 20 min. The devices were completed by thermal deposition of C_{60} (40 nm thick), BCP (8 nm thick), and Ag (100 nm thick) at a vacuum of $< 3 \times 10^{-6}$ Torr. Before measuring the solar cells, PDMS anti-reflection foil was applied on the glass side to minimize the reflection losses. All devices were tested using a Keithley 2400 at room temperature under AM 1.5 G illuminations (1,000 W/m^2) with an Abet Technologies Sun 3000 solar simulator, which was calibrated using a standard silicon cell (RERA). Current-voltage (J–V) curves were obtained both in reverse (1.2 V → − 0.1 V) and forward scan (− 0.1 V → 1.2 V) with a step size of 10 mV and a scan speed of 50 mV/s is used. All the measurements were performed under N_2 environment inside the glovebox. The external quantum efficiency (EQE) of solar cells was measured with a Newport EQE system (Model: Oriel IQE-200) by focusing the chopped monochromatic light beam onto active area of the solar cells without external white-light bias. The maximum power point tracking measurements were performed using Keithley-2400 source meter and in-house tracking program.

3.3. Thin film characterization

A Cary 5000 UV–Vis–NIR spectrophotometer was used to measure absorbance with PTAA coated ITO glass substrates as references. The X-ray diffraction (XRD) patterns were recorded with a Bruker D2 Advance diffractometer (Bruker, PHASER) with Cu Kα radiation (λ = 1.5418 Å). Steady-state photoluminescence (PL) and time-resolved photoluminescence (TRPL) measurements were performed with a spectrofluorometer (Fluoromax-4, Horiba Scientific). For steady-state PL, a 500 nm monochromatic light was continuously illuminated on the surface of the films. For TRPL, a 633 nm pulsed laser was used for the pump excitation and a 760 nm light for the probe. SEM images were obtained with a ZEISS Auriga Crossbeam system with an accelerating voltage of 5 kV. Contact angle measurements were performed with a VCA Optima Contact Angle Measurement system. PTAA and NiO_x surface free energies were calculated from H_2O and DMSO contact angles on these surfaces using the Owens-Wendt-Rabel and Kaelble (OWRK) model. A

Riken AC-2 photo-electron spectrometer was used to measure work-function and ionization potential. Ultraviolet Photoelectron Spectroscopy (UPS) and X-ray Photoelectron Spectroscopy (XPS) measurements were conducted using an Omicron multi-probe Photoemission spectroscopy (PES) system (base pressure of 3×10^{-10} mbar) equipped with a Sphera II EAC 125 hemispherical electron analyzer and a multi-channeltron electron detector. All measurements were carried out in electrical contact to the analyzer without charge neutralization. UPS was carried out at an electron escape angle of 90° with a focus HIS-13 helium discharge lamp with a He(1)α source (21.22 eV) 10^{-1} mbar He (90 mA, 570 V). A minor component (3%) of He(1)β 23.09 eV was deducted from the spectrum to identify the high KE valence band cut-off. A bias of − 9.97 eV was applied to the sample. XPS was carried out at an electron escape angle of 57° with an Al Kα monochromated X-ray source (XM1000) at a power of 390 W. Calibration was made under the same experimental settings and conditions assigning the 0 binding energy position to Fermi level of an evaporated metallic Au reference sample in (UPS) and Fermi level and Au 4f7/2 difference (Δ84.2 eV). The photoelectron pass energy was fixed at 15 eV for high-resolution XPS, 50 eV survey XPS at 5 eV for the valence band region in UPS, and at 10 eV for the Secondary electron cut-off SECO in UPS. An atomic force microscope (AFM) from Bruker (Dimension Icon with ScanAsyst) with a TAP150A (Veeco) cantilever was used to acquire AFM height images. The cantilever had a resonant frequency and stiffness of 129–145 kHz and 5 N/m, respectively. A SOLVER NEXT SPM (NT-MDT) with an atomic force microscopy (AFM) head was used in semi-contact mode to measure topography and surface potential (KPFM). The OSCM-PT (Veeco) cantilever had a resonant frequency of 45–95 kHz and stiffness 0.5–4.4 N/m. The work-function of the tip was found to be 5.07 eV using the contact potential difference (VCPD) of a gold standard (5.1 eV, Veeco) and equation:

$$V_{CPD} = \frac{\phi_{tip} - \phi_{sample}}{e} \quad \text{(M1)}$$

where ϕ is the work-function and e the charge of an electron.

3.4. DFT calculations

All quantum chemical calculations were performed using the Gaussian 09 software package [30]. The molecules were optimized with the B3LYP exchange-correlation functional using a 6–31 + g(d,p) basis set, followed by frequency calculations to confirm the stability of the structures. Interaction energies were calculated at the B3LYP/lanl2dz level of theory as,

$$\mathrm{E} = \mathrm{E}(\mathrm{PTAA} - (\mathrm{DMF/DMSO/NMP} - \mathrm{MAPbI_3})) - \mathrm{E}(\mathrm{PTAA})\text{-}\mathrm{E}(\mathrm{DMF/DMSO/NMP\text{-}MAPbI_3}), \quad \text{(M2)}$$

where E(PTAA-(DMF/DMSO/NMP-$MAPbI_3$)), E(PTAA), and E(DMF/DMSO/NMP-$MAPbI_3$) are the total energies of PTAA interacting with the solvent-$MAPbI_3$ system, isolated PTAA, and the solvent-$MAPbI_3$ system, respectively.

3.5. Characterization of $MAPbI_3$ films and devices

We performed further characterization to obtain insights into the impact of the perovskite inks on the crystallinity and optoelectronic properties of the perovskite absorber. Both $MAPbI_3$ films fabricated using DMF/DMSO (D/D) and DMF/NMP (D/N) based inks exhibit similar X-ray diffraction (XRD) patterns and intensities (Fig. S20). As explained before, Fig. S8 shows $MAPbI_3$(D/D) perovskite having larger grains (for the DMF pre-wetting case), (~300–900 nm) in comparison with $MAPbI_3$(D/N) (~80–100 nm). A slight difference in absorption spectra between both samples can be seen (Fig. S21), resulting in optical band gaps of 1.57 eV (D/D) and 1.59 eV (D/N). Importantly, ultraviolet photoelectron spectroscopy (UPS) measurements indicate that there is a slight shift in the work function of the films from 5.0 eV (D/D) to 5.1 eV (D/N) on PTAA (Fig. S22A). Fig. S22B shows a minimum change in the valence-band maximum (VBM), indicating similar Fermi levels for both the films. Additionally, X-ray photoelectron spectroscopy (XPS) shows no change in core level positions (Fig. S23), indicating an actual change in work function calculated from the ionization energy shift of 5.45 eV (D/D) to 5.55 eV (D/N). Fig. S24 depicts photoelectron spectroscopy in air (PESA) measurements matching very well with the ionization energy from UPS findings. Table S5 tabulates the work-function and ionization potential extracted from different methods for $MAPbI_3$ (D/D) and $MAPbI_3$ (D/N) samples.

Fig. S25 shows atomic force microscopy (AFM) images to compare the peak-to-valley (PtV) distance and root-mean-square (RMS) roughness for both samples. Table S6 tabulates the corresponding values (PtV and RMS) extracted from the images for different scan areas. The RMS roughness increases from 30.9 to 64.8 nm, and the PtV distance from 183.7 to 660 nm, as the scanning area is increased from 1 to 10 μm^2 for $MAPbI_3$(D/D), whereas with $MAPbI_3$(D/N) the RMS roughness increases from 10.6 to 13.4 nm, while the PtV distance increases from 65.7 to 106.7 nm. The values are 3–5 times larger with $MAPbI_3$(D/D) in comparison with $MAPbI_3$(D/N) and vary significantly upon increasing the scan area. Fig. S26 shows the topography and surface potential obtained with kelvin probe force microscopy (KPFM) measurements, with variations in topography similar to that measured by AFM. The PtV distance for $MAPbI_3$(D/D) (225.54 nm), was double the value for $MAPbI_3$(D/N) (104.16 nm) samples over 2 μm^2 due to topographical variations, despite seeking a uniform area with a small PtV distance for the surface-potential maps. The work-function extracted from the average surface potential (KPFM) is 4.98 eV, and 5.07 eV for $MAPbI_3$(D/D) and $MAPbI_3$(D/N), respectively, and the ionization potential (IP) from PESA is estimated to be 5.39 eV and 5.44 eV. Based on these values and from their optical band gaps (Fig. S21), the estimates of electron affinity (EA) are 3.82 eV for $MAPbI_3$(D/D) (E_g~1.57 eV) and 3.85 eV for $MAPbI_3$(D/N) (E_g~1.59 eV). Fig. S27 consolidates the energy band schematic $MAPbI_3$(D/D) and $MAPbI_3$(D/N) layers based on the measurements alongside PTAA and ITO functional layers. The AFM/KPFM measurements show that the DMF/DMSO ink produces a rough $MAPbI_3$ film with loosely packed grains when deposited on the hydrophobic PTAA. Based on these measurements, we expect a higher trap-state density for PSCs fabricated using $MAPbI_3$(D/D) absorber in comparison to $MAPbI_3$(D/N) based devices. Fig. S28 shows the space-charge-limited-current (SCLC) measurements, where $MAPbI_3$(D/D) PSC exhibits a higher trap density (1.29×10^{16} cm^{-3}) than that of $MAPbI_3$(D/N) PSC (1.11×10^{16} cm^{-3}). The increased trap-state density of the $MAPbI_3$(D/D) PSC is consistent with their device performance, as they deliver ~80 mV lower open circuit potential (V_{OC}) than the NMP counterpart.

4. Conclusions

This work combines experimental results with DFT calculations to systematically investigate the ink interaction on a hydrophobic surface towards perovskite film formation. We identify the low binding energy and weak electronic interaction of $MA^+PbI_3^-$•DMSO adduct on the PTAA surface to be the main culprit for the crystallization and formation of micro- and nano-scale pinholes. These insights lead us to NMP as a suitable alternative. The comprehensive understanding of the ink-substrate interaction enables continuing device advancements in scalability on a multitude of charge-transporting layers.

Funding

This publication is based upon work supported by the King Abdullah University of Science and Technology (KAUST) Office of Sponsored Research (OSR) under Award No. OSR-2019-CARF/CCF-3097.

CRediT authorship contribution statement

Furkan H. Isikgor: Conceptualization, Methodology, Validation, Formal analysis, Investigation, Data curation, Writing - original draft, Visualization, Supervision. **Anand S. Subbiah**: Methodology, Validation, Formal analysis, Investigation, Data curation, Writing - original draft. **Mathan K. Eswaran**: Methodology, Software, Validation, Formal analysis. **Calvyn T. Howells**: Formal analysis, Investigation, Writing - original draft. **Aslihan Babayigit**: Writing - original draft. **Michele De Bastiani**: Investigation, Writing - review & editing. **Emre Yengel**: Investigation, Writing - review & editing. **Jiang Liu**: Investigation, Writing - review & editing. **Francesco Furlan**: Validation, Investigation. **George T. Harrison**: Formal analysis, Investigation, Writing - review & editing. **Shynggys Zhumagali**: Validation, Investigation. **Jafar I. Khan** : Investigation, Writing - review & editing. **Frédéric Laquai**: Validation, Writing - review & editing. **Thomas D. Anthopoulos**: Validation, Writing - review & editing. **Iain McCulloch**: Validation, Writing - review & editing. **Udo Schwingenschlögl**: Validation, Writing - review & editing. **Stefaan De Wolf**: Validation, Writing - original draft, Visualization, Supervision, Project administration, Funding acquisition.

Declaration of Competing Interest

The authors declare that they have no known competing financial interests or personal relationships that could have appeared to influence the work reported in this paper.

Acknowledgements

The authors thank the members of the KAUST solar center operations team for their technical help and support as well as Thomas G. Allen, Erkan Aydin and Emmanuel Van Kerschaver for fruitful discussions.

Appendix A. Supporting information

Supplementary data associated with this article can be found in the online version at doi:10.1016/j.nanoen.2020.105633.

References

[1] National Renewable Energy Laboratory, Best research-cell efficiencies, (Accessed: May 2020), ⟨https://www.nrel.gov/pv/cell-efficiency.html⟩.
[2] F. Huang, M. Li, P. Siffalovic, G. Cao, J. Tian, From scalable solution fabrication of perovskite films towards commercialization of solar cells, Energy Environ. Sci. 12 (2019) 518–549, https://doi.org/10.1039/C8EE03025A.
[3] L. Qiu, S. He, L.K. Ono, S. Liu, Y. Qi, Scalable fabrication of metal halide perovskite solar cells and modules, ACS Energy Lett. 4 (2019) 2147–2167, https://doi.org/10.1021/acsenergylett.9b01396.
[4] Z. Li, T.R. Klein, D.H. Kim, M. Yang, J.J. Berry, M.F.A.M. van Hest, K. Zhu, Scalable fabrication of perovskite solar cells, Nat. Rev. Mater. 3 (2018) 18017–18037, https://doi.org/10.1038/natrevmats.2018.17.
[5] M. Zhang, B. Wilkinson, Y. Liao, J. Zheng, C.F.J. Lau, J. Kim, J. Bing, M.A. Green, S. Huang, A.W.-Y. Ho-Baillie, Electrode design to overcome substrate transparency limitations for highly efficient 1 cm^2 mesoscopic perovskite solar cells, Joule 2 (2018) 2694–2705, https://doi.org/10.1016/j.joule.2018.08.012.
[6] D.H. Kim, J.B. Whitaker, Z. Li, M.F.A.M. van Hest, K. Zhu, Outlook and challenges of perovskite solar cells toward terawatt-scale photovoltaic module technology, Joule 2 (2018) 1437–1451, https://doi.org/10.1016/j.joule.2018.05.011.
[7] L.K. Ono, N.-G. Park, K. Zhu, W. Huang, Y. Qi, Perovskite solar cells—towards commercialization, ACS Energy Lett. 2 (2017) 1749–1751, https://doi.org/10.1021/acsenergylett.7b00517.
[8] T. Liu, K. Chen, Q. Hu, R. Zhu, Q. Gong, Inverted perovskite solar cells: progresses and perspectives, Adv. Energy Mater. 6 (2016) 1600457–1600474, https://doi.org/10.1002/aenm.201600457.
[9] H. Kim, K.-G. Lim, T.-W. Lee, Planar heterojunction organometal halide perovskite solar cells: roles of interfacial layers, Energy Environ. Sci. 9 (2016) 12–30, https://doi.org/10.1039/C5EE02194D.
[10] X. Liu, Y. Cheng, C. Liu, T. Zhang, N. Zhang, S. Zhang, J. Chen, Q. Xu, J. Ouyang, H. Gong, 20.7% highly reproducible inverted planar perovskite solar cells with enhanced fill factor and eliminated hysteresis, Energy Environ. Sci. 12 (2019) 1622–1633, https://doi.org/10.1039/C9EE00872A.
[11] S. Hong, J. Lee, H. Kang, G. Kim, S. Kee, J.-H. Lee, S. Jung, B. Park, S. Kim, H. Back, K. Yu, K. Lee, High-efficiency large-area perovskite photovoltaic modules achieved via electrochemically assembled metal-filamentary nanoelectrodes, Sci. Adv. 4 (2018), eaat3604, https://doi.org/10.1126/sciadv.aat3604.
[12] C. Bi, Q. Wang, Y. Shao, Y. Yuan, Z. Xiao, J. Huang, Non-wetting surface-driven high-aspect-ratio crystalline grain growth for efficient hybrid perovskite solar cells, Nat. Commun. 6 (2015) 7747, https://doi.org/10.1038/ncomms8747.
[13] F. Zhang, J. Song, R. Hu, Y. Xiang, J. He, Y. Hao, J. Lian, B. Zhang, P. Zeng, J. Qu, Interfacial passivation of the p-doped hole-transporting layer using general insulating polymers for high-performance inverted perovskite solar cells, Small 14 (2018), 1704007, https://doi.org/10.1002/smll.201704007.
[14] M. Stolterfoht, C.M. Wolff, J.A. Márquez, S. Zhang, C.J. Hages, D. Rothhardt, S. Albrecht, P.L. Burn, P. Meredith, T. Unold, D. Neher, Visualization and suppression of interfacial recombination for high-efficiency large-area pin perovskite solar cells, Nat. Energy 3 (2018) 847–854, https://doi.org/10.1038/s41560-018-0219-8.
[15] K.O. Brinkmann, J. He, F. Schubert, J. Malerczyk, C. Kreusel, F. van gen Hassend, S. Weber, J. Song, J. Qu, T. Riedl, Extremely robust gas-quenching deposition of halide perovskites on top of hydrophobic hole transport materials for inverted (p–i–n) solar cells by targeting the precursor wetting issue, ACS Appl. Mater. Interfaces 11 (2019) 40172–40179, https://doi.org/10.1021/acsami.9b15867.
[16] H.X. Dang, K. Wang, M. Ghasemi, M.-C. Tang, M. De Bastiani, E. Aydin, E. Dauzon, D. Barrit, J. Peng, D.-M. Smilgies, S. De Wolf, A. Amassian, Multi-cation synergy suppresses phase segregation in mixed-halide perovskites, Joule 3 (2019) 1746–1764, https://doi.org/10.1016/j.joule.2019.05.016.
[17] K. Wang, M.-C. Tang, H.X. Dang, R. Munir, D. Barrit, M. De Bastiani, E. Aydin, D.-M. Smilgies, S. De Wolf, A. Amassian, Kinetic stabilization of the sol–gel state in perovskites enables facile processing of high-efficiency solar cells, Adv. Mater. 31 (2019), 1808357, https://doi.org/10.1002/adma.201808357.
[18] J.-W. Lee, Z. Dai, C. Lee, H.M. Lee, T.-H. Han, N. De Marco, O. Lin, C.S. Choi, B. Dunn, J. Koh, D. Di Carlo, J.H. Ko, H.D. Maynard, Y. Yang, Tuning molecular interactions for highly reproducible and efficient formamidinium perovskite solar cells via adduct approach, J. Am. Chem. Soc. 140 (2018) 6317–6324, https://doi.org/10.1021/jacs.8b01037.
[19] M. Saliba, J.-P. Correa-Baena, C.M. Wolff, M. Stolterfoht, N. Phung, S. Albrecht, D. Neher, A. Abate, How to make over 20% efficient perovskite solar cells in regular (n–i–p) and inverted (p–i–n) architectures, Chem. Mater. 30 (2018) 4193–4201, https://doi.org/10.1021/acs.chemmater.8b00136.
[20] M. Jung, S.-G. Ji, G. Kim, S.I. Seok, Perovskite precursor solution chemistry: from fundamentals to photovoltaic applications, Chem. Soc. Rev. 48 (2019) 2011–2038, https://doi.org/10.1039/C8CS00656C.
[21] N.J. Jeon, J.H. Noh, Y.C. Kim, W.S. Yang, S. Ryu, S.I. Seok, Solvent engineering for high-performance inorganic–organic hybrid perovskite solar cells, Nat. Mater. 13 (2014) 897–903, https://doi.org/10.1038/nmat4014.
[22] F.H. Isikgor, B. Li, H. Zhu, Q. Xu, J. Ouyang, High performance planar perovskite solar cells with a perovskite of mixed organic cations and mixed halides, $MA_{1-x}FA_xPbI_{3-y}Cl_y$, J. Mater. Chem. A 4 (2016) 12543–12553, https://doi.org/10.1039/C6TA03381D.
[23] A.S. Al-Jimaz, M.S. Fandary, K.H.A.E. Alkhaldi, J.A. Al-Kandary, M.A. Fahim, Extraction of aromatics from middle distillate using n-methyl-2-pyrrolidone: experiment, modeling, and optimization, Ind. Eng. Chem. Res. 46 (2007) 5686–5696, https://doi.org/10.1021/ie060960f.
[24] Y. Zhou, O.S. Game, S. Pang, N.P. Padture, Microstructures of organometal trihalide perovskites for solar cells: their evolution from solutions and characterization, J. Phys. Chem. Lett. 6 (2015) 4827–4839, https://doi.org/10.1021/acs.jpclett.5b01843.
[25] H. Hu, M. Singh, X. Wan, J. Tang, C.-W. Chu, G. Li, Nucleation and crystal growth control for scalable solution-processed organic–inorganic hybrid perovskite solar cells, J. Mater. Chem. A 8 (2020) 1578–1603, https://doi.org/10.1039/C9TA11245F.
[26] D. Luo, W. Yang, Z. Wang, A. Sadhanala, Q. Hu, R. Su, R. Shivanna, G.F. Trindade, J.F. Watts, Z. Xu, T. Liu, K. Chen, F. Ye, P. Wu, L. Zhao, J. Wu, Y. Tu, Y. Zhang, X. Yang, W. Zhang, R.H. Friend, Q. Gong, H.J. Snaith, R. Zhu, Enhanced photovoltage for inverted planar heterojunction perovskite solar cells, Science 360 (2018) 1442–1446, https://doi.org/10.1126/science.aap9282.
[27] H.D. Kim, H. Ohkita, H. Benten, S. Ito, Photovoltaic performance of perovskite solar cells with different grain sizes, Adv. Mater. 28 (2016) 917–922, https://doi.org/10.1002/adma.201504144.
[28] M.A. Haque, J. Troughton, D. Baran, Processing-performance evolution of perovskite solar cells: from large grain polycrystalline films to single crystals, Adv. Energy Mater. 10 (2020), 1902762, https://doi.org/10.1002/aenm.201902762.
[29] Z. Chu, M. Yang, P. Schulz, D. Wu, X. Ma, E. Seifert, L. Sun, X. Li, K. Zhu, K. Lai, Impact of grain boundaries on efficiency and stability of organic-inorganic trihalide perovskites, Nat. Commun. 8 (2017) 2230, https://doi.org/10.1038/s41467-017-02331-4.
[30] G.W. T.M. J. Frisch, H.B. Schlegel, G.E. Scuseria,M.A. Robb, J.R., G.S. Cheeseman, V. Barone, B. Mennucci,G.A. Petersson, H. Nakatsuji, M., X.L. Caricato, H.P. Hratchian, A.F. Izmaylov, J. Bloino, G. Zheng, J.L., M.H. Sonnenberg, M. Ehara, K. Toyota, R. Fukuda, J. Hasegawa, M. Ishida, T., Y.H. Nakajima, O. Kitao, H. Nakai, T. Vreven, J.A. Montgomery, Jr.,J.E., F.O. Peralta, M. Bearpark, J.J. Heyd, E. Brothers, K.N. Kudin, V.N., T.K. Staroverov, R. Kobayashi, J. Normand,K. Raghavachari, A. Rendell, J.C., S.S. I. Burant, J. Tomasi,M. Cossi, N. Rega, J.M. Millam, M. Klene, J.E., J.B. C. Knox, V. Bakken, C. Adamo, J. Jaramillo, R. Gomperts, R.E., O.Y. Stratmann, A.J. Austin, R. Cammi, C. Pomelli, J.W. Ochterski, R.L., K.M. Martin, V.G. Zakrzewski, G.A. Voth, P. Salvador, J.J. Dannenberg, A.D. D.S. Dapprich, O. Farkas, J.B. Foresman, J.V. Ortiz, J. Cioslowski,and, D.J. Fox, Gaussian, Gaussian, Inc., Wallingford CT, (2013), Gaussian 09, Revision D.01.

Furkan H. Isikgor received his Integrated BS and MS degree in Chemistry Education from Boğaziçi University, Istanbul, Turkey. He also completed his M.Sc. at Boğaziçi University, during which time he worked on the synthesis, HPLC, and NMP studies on axially chiral molecules. He received his Ph.D. degree from the National University of Singapore in 2018. His Ph. D. thesis was based on "Novel hybrid organic–inorganic perovskite materials and solar cells". He is currently a post-doctoral fellow at KAUST Solar Center, working on wide-bandgap single-junction perovskite solar cells and perovskite/silicon tandem solar cells.

Anand S. Subbiah is currently a post-doctoral research fellow in Prof. Stefaan De Wolf group at King Abdullah University of Science and Technology (KAUST), Saudi Arabia. Originally from Tamil Nadu, India he completed his MTech, in Nanotechnology from PSG CT (TN, India) and Ph.D. in Energy Engineering from IIT Bombay (MH, India) under the supervision of Prof. Shaibal Sarkar. His current research interests are towards the scalable fabrication of perovskite solar cells and silicon-perovskite tandems using solution processing techniques.

Mathan K. Eswaran received his Ph.D. from SRM Institute of Technology, India in 2018. He is currently working as a Post-Doctoral researcher at King Abdullah University of Science and Technology, Saudi Arabia. His research work is primarily focused on first-principles investigation of hybrid materials for application in solar cells and Pt-free catalysts for CO_2 conversion and exploring the properties of carbon based allotropes for energy storage applications.

Calvyn Howells holds a M.Sci (University of Strathclyde) and Ph.D. (University of St Andrews) in Physics. His Ph.D. focussed on organic photovoltaics and was completed under the supervision of Professors Ifor Samuel and Graham Turnbull. After a few years in Oil and Gas as a geophysicist (CGG) he started a postdoctoral research career. His last fellowship was at King Abdullah University of Science and Technology (KAUST) under Professor Iain McCulloch where he predominately researched solar to hydrogen conversion. Calvyn is interested in novel materials for energy-related applications and is now part of the research laboratory team at Khalifa University (KUSTAR).

Aslihan Babayigit studied Biomedical Sciences at Hasselt University (BE) in 2013. Completing her Bachelor degree with a Master in Bioelectronics and Nanotechnology in 2015, she currently is a Ph.D. fellow of Research Fund Flanders (FWO) pursuing a Doctorate in Sciences in the Nanostructure Physics Group at the Institute for Materials Research (IMO-IMOMEC) of Hasselt University and IMEC (BE). Her core focus is perovskite photovoltaics—on the device level and the material level. More generally, her interests include the electro-optical characterization of nanostructured materials for applications in energy and life sciences.

Michele De Bastiani obtained his MSc (2011) in material science at the Universita' degli Studi di Padova and his Ph.D. (2016) in the School of Material Science and Engineering of the Universita' degli Studi di Padova, in co-tutelage with the Center for Nanoscience and Technology (CNST) of the Istituto Italiano di Tecnologia, in Milan, Italy. After his Ph.D., he joined the King Abdullah University of Science and Technology (KAUST), Jeddah, Kingdom of Saudi Arabia. His research focuses the development and scaling-up of efficient and stable perovskite/silicon tandem with particular interest in test-field experiments.

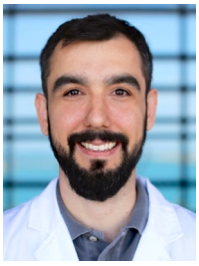

Emre Yengel is a senior researcher in Laboratory of Applied Materials and Applications at King Abdullah University of Science and Technology (KAUST) in Saudi Arabia. He completed his Ph.D. in electrical engineering at University of California, Riverside (USA) followed by a postdoctoral fellowship in University of California, Davis (USA). His research focuses on new materials and structures for optoelectronic applications in nanogap devices including photovoltaics, photodiodes and LEDs as well as oxide semiconductor thin-film transistors.

Jiang Liu received his Bachelor degree from Hunan University, China in 2008, and obtained his Ph.D. degree in Material Science and Engineering from Tsinghua University, China in 2013. Currently, He is a postdoctoral fellow in Stefaan De Wolf Group in King Abdullah University of Science and Technology. His research interest includes perovskite-based solar cells and perovskite/Si tandem solar cells.

Francesco Furlan received his master's degree from Padua University in 2019. After spending one year at King Abdullah University of Science and Technology as a visiting student, he is now a Ph.D. candidate at Imperial College, London. His main research interests are the study of novel semiconducting materials and the development of devices for optoelectronic applications.

George T. Harrison completed B.Sc. (Hons) in Chemistry at Manchester University. Studying for MSc and Ph.D. at University College London; completing PhD in the group of Prof. Geoff Thornton in the field of surface science of TiO_2. He is currently a post-doc in Stefaan De Wolf's group at KAUST Solar Centre specializing in interface analysis employing photoemission methods of photovoltaic devices.

Shynggys Zhumagali received his MSc in Chemistry degree at Ulsan National University of Science and Technology. He is currently a Ph.D. student under the supervision of Prof. Stefaan De Wolf in the department of Materials Science and Engineering of King Abdullah University of Science and Technology. His research interests focus on developing new technologies in all perovskite tandem and single-junction solar cells.

Jafar I. Khan is a Research Scientist at King Abdullah University of Science and Technology (KAUST), Saudi Arabia, since 2018. He graduated from University of Copenhagen, Niels Bohr Institute, Denmark, in Physics in 2004 with M.Sc, afterwards he completed his PhD from The University of Leeds, UK, in 2010. He continued as a post-doc at The University of Leeds, and subsequently, moved to KAUST in 2013 as a post-doctoral fellow. Jafar's research is focused on ultrafast time resolved spectroscopy of energy harvesting materials, specifically photophysics of organic and hybrid materials.

Frédéric Laquai graduated in Physical Chemistry from the University of Marburg, Germany, in 2003. He received a doctoral degree with distinction in Physical Chemistry from the University of Mainz (Germany) in 2006. After a two-years postdoctoral stay at the Cavendish Laboratory in Cambridge (UK), he moved to the Max Planck Institute for Polymer Research in Mainz, Germany, to become a Max Planck Research Group Leader. In 2015, he moved to KAUST as Associate Professor of Material Science and Physics. Frédéric's research focuses on the photophysics of materials for solar energy conversion.

Thomas D. Anthopoulos is a professor of material science and engineering at King Abdullah University of Science and Technology (KAUST) in Saudi Arabia. He received his B.Eng. and D. Phil. degrees from Staffordshire University in the UK followed by postdoctoral appointments at the University of St. Andrews (UK) and Philips Research Laboratories (The Netherlands) before joining Imperial College London (UK) from 2006 to 2017. His research interests are diverse and cover the development and application of innovative processing paradigms and the physics, chemistry, and application of functional materials.

Iain McCulloch is a polymer chemist, currently a Professor in the Chemistry Department at the University of Oxford in the UK, as well as Director of KAUST Solar Center in Saudi Arabia, where he is also a Professor of Chemical Science. Iain is a Fellow of the Royal Society, a Member of Academia Europaea, a Fellow of the European Academy of Sciences and a Fellow of the Royal Society of Chemistry. He has received the Royal Society of Chemistry 2020 Interdisciplinary Prize, the 2016 Tilden Prize, and the 2009 Creativity in Industry Prize. In 2020, he was also awarded the European Academy of Sciences Blaise Pascal Medal for Materials Science.

Udo Schwingenschlögl is a Professor of Applied Physics at King Abdullah University of Science and Technology (KAUST). He joined KAUST as founding faculty member in 2008. His research interests in condensed matter physics and first-principles materials modeling focus on two-dimensional materials, interface and defect physics, correlated materials, thermoelectric materials, metal-ion batteries, nanoparticles, and quantum transport.

Stefaan De Wolf received his PhD degree in 2005 from the Katholieke Universiteit Leuven, during which time he was also affiliated with IMEC in Belgium. From 2005 to 2008, he was with the National Institute of Advanced Industrial Science and Technology (AIST), Japan. In 2008, he joined the Photovoltaics and Thin-Film Electronics Laboratory, Ecole Polytechnique Federale de Lausanne (EPFL), Switzerland, as a team leader. Since 2016, he is an associate professor at the King Abdullah University of Science and Technology (KAUST), Saudi Arabia, focusing silicon and perovskite solar cells, perovskite/silicon tandem solar cells, and photovoltaics for sunny and hot climates.